



Full Text View

[Volume 29, Issue 11 \(November 1999\)](#)

Journal of Physical Oceanography

Article: pp. 2829–2850 | [Abstract](#) | [PDF \(452K\)](#)

Directional Response of Wind Waves to a Large Wind Shift

Frederick C. Jackson

Alexandria, Virginia

Robert E. Jensen

U.S. Army Corps of Engineers, Vicksburg, Mississippi

(Manuscript received June 3, 1998, in final form December 21, 1998)

DOI: 10.1175/1520-0485(1999)029<2829:DROWWT>2.0.CO;2

ABSTRACT

The directional response of a fully arisen sea to a $\sim 90^\circ$ wind shift is studied using a combination of airborne radar and in situ directional wave observations. The observations were made in February 1991 as a part of the Surface Wave Dynamics Experiment. Radar and buoy mean wave directions in several frequency bands are polynomial-smoothed in fetch and duration coordinates and analyzed for the directional relaxation parameter b by using finite differences of the gridded, smoothed data in a one-dimensional advection equation for the mean wave direction. The analysis is carried out using several different sets of buoy wind and wave data in an event window of 40 h in duration by 200 km in fetch (100–300 km offshore). For the most well-populated and reliable inverse wave age class in the study, $1.2 \leq U/c < 1.6$, the authors find $b = 3.3(\pm 0.1) \times 10^{-5}$. The data do not support any inference as to possible wave age dependence other than, perhaps, the null hypothesis, $b = \text{const} (U/c)$. Frequencies near the spectral peak do not respond according to the relaxation model, and misleading values of b may result from a standard analysis of the data. Wave–current interactions are a potential source of bias. Reflected waves in the study area may be biasing the present result low by as much as 20%.

1. Introduction

Measurements of the directional response of ocean waves to turning winds are important for assessing numerical wave model performance. In the third-generation (3-G) wave models that incorporate nonlinear wave physics ([WAMDI Group 1988](#)) such measurements are particularly important for determining whether the physical

Table of Contents:

- [Introduction](#)
- [Observations](#)
- [Analysis](#)
- [Results](#)
- [Discussion](#)
- [Conclusions](#)
- [REFERENCES](#)
- [APPENDIX](#)
- [TABLES](#)
- [FIGURES](#)

Options:

- [Create Reference](#)
- [Email this Article](#)
- [Add to MyArchive](#)
- [Search AMS Glossary](#)

Search CrossRef for:

- [Articles Citing This Article](#)

Search Google Scholar for:

- [Frederick C. Jackson](#)
- [Robert E. Jensen](#)

parameterizations are correctly representing the actual physics. Measurements of wave growth for a constant (i.e., step function) driving wind have fairly well established 3-G model performance in terms of the predicted wave–energy growth and spectral downshifting of the peak frequency with duration or fetch. The same cannot be said, however, in the case of the model directional spectrum response to wind direction changes. Here model validation has been hindered by a lack of consensus among the measurements of the directional relaxation parameter ([van Vledder and Holthuijsen 1993](#)).

The measurements of [Hasselmann et al. \(1980\)](#) are among the earliest reported measurements of the wave directional response to turning winds. Hasselmann et al. proposed the now familiar relaxation model as a convenient way to parameterize the directional response. According to this model, the mean wave direction $\bar{\theta}_f$ for any frequency f relaxes toward the (new) wind direction θ_w as

$$d\bar{\theta}_f/dt = 2\pi b f \sin(\theta_w - \bar{\theta}_f), (1)$$

where b is the directional relaxation parameter. The wave directional response at any frequency is thus to be characterized by a single integral timescale,

$$\tau_f = 1/(2\pi b f). (2)$$

The relaxation parameter may or may not be a function of nondimensional wave frequency or of wave age, c/U , where $c = g/(2\pi f)$ is the wave phase speed and U is the wind speed (g being acceleration of gravity). [Hasselmann et al. \(1980\)](#) applied the above relaxation model to several wind turning events in which the wind shifts could be described as either more or less steplike or continuously rotating in nature. From a one parameter regression analysis, they found for the inverse wave age range that exhibited the highest correlation, $1.2 \leq U/c < 1.6$, a value of $b = 2.4(\pm 0.5) \times 10^{-5}$. A number of subsequent studies have applied this model to both field observations ([Allender et al. 1983](#); [Masson 1990](#)) and to artificially generated wave model data ([Young et al. 1987](#)). An alternative model of the wave directional response based on the predictive equations of a second-generation (2-G) parametric type wave model was proposed by [Gunther et al. \(1981\)](#). In this model, only the dominant wave response is parameterized. If $\bar{\theta}_o$ is the momentum-weighted overall mean direction, then according to this model,

$$d\bar{\theta}_o/dt = (\chi f_m^2 U/g) \sin(\theta_w - \bar{\theta}_o), (3)$$

where f_m is the peak frequency of the windsea. This formulation of the directional relaxation has also been used in a number of subsequent studies, including those of [Holthuijsen et al. \(1987\)](#) and [van Vledder and Holthuijsen and \(1993\)](#). A summary of the published data on the relaxation parameter, including both b and χ forms, can be found in the latter reference.

As can be seen from [Table 3](#) of [van Vledder and Holthuijsen \(1993\)](#) (and cf. our [Table 4](#)) there is considerable disagreement among a number of the estimates of the relaxation parameter. [Van Vledder and Holthuijsen \(1993\)](#) ascribe the discrepancy to biases associated with the data selection criteria and analysis procedures employed in the individual investigations. That such biases exist there is no question. What is not clear, however, is to whose data they should be ascribed. The present study was undertaken in the hope that the new data it provides might help to resolve this dilemma.

In this study mean direction data are derived from a combination of airborne radar and in situ directional wave observations. The data were collected during the Surface Wave Dynamics Experiment (SWADE) in February 1991. The combination of the areally extensive radar data and temporally dense buoy data permits advective effects to be addressed. Heretofore, only [van Vledder and Holthuijsen \(1993\)](#) seem to have applied advection corrections to the data on directional relaxation. However, these were based on model hindcast data rather than on actual observations. [Section 2](#) describes our observations. [Section 3](#) describes the data analysis. [Section 4](#) presents the results. [Section 5](#) discusses them and compares them to the published data.


2. Observations

The data reported here were acquired as a part of SWADE, which took place off the east coast of the United States in winter–spring 1990/91 ([Weller et al. 1991](#)). During the latter part of the experiment, shortly before the start of the Third Intensive Observational Period (Caruso et al. 1994), four special flights of NASA's airborne Radar Ocean Wave Spectrometer (ROWS) instrument were conducted to observe the wave field response to a significant winter frontal event. The four aircraft flights took place between ca. 1800 UTC 14 February and 1600 UTC 16 February 1991. The wind/wave event is described in detail by [Jackson and Jensen \(1995\)](#). This paper also details the data collection and data analysis procedures used to obtain the data used in the present study. A yet more complete description of the data collection and analysis procedures as well as complete set of data for this event, including both radar and buoy estimated directional

spectra, can be found in a SWADE data report ([Jackson 1996](#)).

a. Data sources

1) RADAR DATA

[Figure 1](#)  shows the aircraft flight lines and the locations of the radar observations for the four ROWS flights between 14 and 16 February 1991. These flight-line maps also show the SWADE data buoy locations and model current fields for each flight day. On these maps, an “S” denotes a radar wave spectrum observation and an “A” denotes a wind speed observation, which is made from another of the instrument’s operating modes (altimeter mode). The radar was operated at a constant pressure altitude of 7625 m. Data files are 100 s long and consist of backscattered power data from 10 revolutions of the conically scanning antenna. The radar spectra are produced from the observed quasi-symmetric directional slope (radar reflectivity) spectra in the wavenumber domain by first folding the directional spectra about an arbitrary axis and then transforming to the frequency domain assuming the linear, deep water dispersion relationship. The polar-symmetric directional spectra so produced have 40 degrees of freedom per elementary frequency and direction band. The directional and wavenumber resolutions are of the order of 30° or better and 20% or better for waves shorter than 200 m. The radar response is fairly linear on wave slopes for frequencies up to 0.20 Hz. Scattering nonlinearities are generally small enough that their effects are masked by larger spectral power contributions from antenna pattern and aircraft motion effects (finite data window effects) and residual speckle noise. These effects can be particularly troublesome for the measurement of spectra of windseas with wave heights less than 2 m or so. This is one of the reasons why we will limit our use of the radar data in this study to fetches >125 km (see appendix B for details).


Mean direction can be derived directly from the radar directional energy spectrum data simply by taking the first angular moment of the spectrum. However, the 180° directional ambiguity inherent to radar measurement introduces an unwanted dependence of the moment result on an arbitrary choice of a folding or symmetry axis. The same applies to the first harmonic phase angle since, once again, one must make an assumption as to which half space contains the true directions of wave travel. The second angular harmonic, on the other hand, is insensitive to the 180° ambiguity. Comparison of these three estimators of mean direction, namely, the first angular moment and the first and second angular harmonic estimators, shows the second harmonic estimator to produce the most stable estimates. Moreover, it is found that the second harmonic estimates tend to lie intermediate between the two other estimates. From the polar symmetric radar energy spectrum data $E(f, \theta)$, the mean direction is thus to be estimated according to



$$\bar{\theta}_f = \frac{1}{2} \arg\left(\int_0^{2\pi} e^{i2\theta} E(f, \theta) d\theta\right), \quad (4)$$

where the correct quadrant is to be determined from the synoptic situation and/or consideration of spatial continuity.

2) BUOY DATA

Consistently with the radar data, buoy mean directions are taken to be the second harmonic phase angles. These data are taken from the NDBC (National Data Buoy Center) harmonic coefficient data in the SWADE data archive at NASA’s Wallops Flight Facility ([Oberholtzer and Donelan 1996](#)). Buoy directional spreading data are also derived from these records (see section 3a). Buoy directional spectra produced by the maximum likelihood method (MLM) are also available in the SWADE data archive. Plots of these MLM spectra for the period under study are given in the referenced data report ([Jackson 1996](#)).

Four directional wave-sensing buoys formed the heart of the SWADE experiment. These buoys, designated Discus-N (orth), Discus-E(ast), Discus-C(entral), and Buoy CERC, were located 100–175 km offshore of NASA’s Wallops Flight Facility on Virginia’s Eastern Shore in the southern portion of the Middle Atlantic Bight, as shown in [Fig. 1](#) . Since the wave data from Discus-E are strongly affected by the Gulf Stream [the buoy was physically entrained in the current; see section 2c and appendix A] and Buoy CERC is located too far south to be very useful for this particular study, we will be using wave data only from Discus-N and Discus-C. Wind data on the other hand are taken from all four directional wave-sensing buoys and, in addition, from the EXP buoy (WMO buoy number 44024), which was located just shoreward of Discus-C.

The winds used in this study are the buoy-recorded winds reduced to neutral equivalent 10-m values U_{10n} according to the boundary layer model of [Large and Pond \(1981\)](#). [Figure 2](#)  shows the buoy wind histories for the event. In the analysis to follow, we will be using two representative wind histories, one from Discus-E alone, and the other a vector average of the winds from all five of the aforementioned buoys. Discus-E is chosen because it is the most seaward and the most centrally located of the data buoys with respect to the analysis domain of this study. From [Fig. 2](#)  it is seen that the

Discus-E winds are for the most part higher by several meters per second than the five-buoy average winds, which are weighted in favor of the four buoys closer to shore. Higher winds in the central portion of the study area are also indicated by the ROWS wind speed observations (see [Figs. 8](#) and [Fig. 9](#) in [Jackson and Jensen 1995](#) and [Jackson 1996](#)).

b. The wind/wave event

The wave field in the SWADE experiment area in the southern Middle Atlantic Bight (MAB) consisted initially, on 14 February, of a relatively fresh, northward-directed 12-s swell system generated earlier in a region of strong winds to the south of Cape Hatteras. Although technically swell, this wave system has suffered very little decay and still has the character of a fully developed sea ([Jackson and Jensen 1995](#)). The winds at the time of the first radar flight on 14 February, just prior to the passage of the first of two back-to-back cold fronts, were approximately 10 m s^{-1} from the southwest. On the south side of the Gulf Stream, the wave system is northward-directed at all frequencies. After passing through the eastward-directed portion of the Gulf Stream and the local southwesterly wind field in the SWADE area, the system shows a turning with frequency into the local wind direction toward the northwest. With the passage of the first front around 1900 UTC 14 February, the southwesterly winds start to shift to westerly. The front is marked by an absolute pressure minimum of ~ 980 mb and a local (warm side) wind maximum of $\sim 12 \text{ m s}^{-1}$ from the southwest. Following the passage of this first front the winds continue to turn to a westerly direction but diminish in intensity as a trough region moves through the area. Around 0600 UTC on the 15th, a second cold front appears behind the trough, and the winds start to pick up from the west, soon reaching about 12 m s^{-1} . These westerly winds persist until around the time of the third aircraft flight when the winds pick up some more and slowly become more northwesterly. Wind speeds have a sustained maximum of over 15 m s^{-1} for most of the period between 0300 and 1600 UTC on the 16th, after which point the winds start to slacken. By the time of the fourth aircraft flight on the 16th, the initially northward-traveling wave system has been transformed into a purely fetch-limited windsea growing under the fairly steady northwesterly winds. Examples of directional spectra for all phases of the wind/wave event are given in [Jackson and Jensen \(1995\)](#), and the complete set of radar and buoy spectra for the event are given in [Jackson \(1996\)](#).

c. Wave-current interaction

The Gulf Stream came unusually close to shore during the study period. As seen in [Fig. 1](#), the current starts meandering sharply on leaving Cape Hatteras. Entering the southern MAB, it comes close to the mouth of Chesapeake Bay before turning eastward. Buoy CERC and Discus-E both are situated on the current's inshore, cyclonic margin. Physical contact with the current is evident in both of these buoy temperature records. Discus-E was actually entrained by the current and dragged approximately 40 km northeast from its original mooring location to the location shown in [Fig. 1](#). As discussed in appendix A, wave data from this buoy appear to be corrupted by the current, particularly during the middle of the event, on 15 February. For this reason, wave data from Discus-E will not be used in the present study.

The principal effects of the current on the wave field in the study area appear to be 1) the creation of a wave shadow zone starting around the shelf break and including the area inshore of the shelf break for the initial, northward-traveling system and 2) the creation of a reflected system of waves north of the Gulf Stream later in the event for the newly generated, southeastward directed, fetch-limited waves. ROWS data for the two flights on 14 February show a sharp decline in energy of the northward-directed swell system inshore of about 100 km, which is consistent with refraction by a sinusoidal-like meander ([Liu et al. 1989](#), [Fig. 9h](#)). Shay et al. (1995) provide detailed refraction calculations for the Gulf Stream in the southern MAB during the SWADE experiment, which show the creation of a wave shadow zone near the coast. On the northern leg of the first radar flight on 14 February, there is a tenfold drop in energy as one proceeds from file S04 seaward of Discus-N to file S02 inshore of Discus-N, and on the southern leg of the same flight there is a fourfold decrease in wave energy between files S13 and S14. On the second flight, the effect is less dramatic, with a factor of 2 to 4 decrease in wave energy in the vicinity of the shelf break. Similar wave refraction effects are observed by [Walsh et al. \(1996\)](#) in closely spaced airborne radar wave observations that were made in the same area during SWADE some three weeks after the present observations. The calculations of [Shay et al. \(1996\)](#) made in support of these observations show that the refraction pattern is very sensitive to the precise attack angle of the northward-traveling system. Partial shadowing results for waves traveling to 0° true while complete shadowing of the shelf region results for incident waves traveling to 10° . In this case there is a strong caustic formation at the wave shadow region boundary in the vicinity of the shelf break.

Examination of the detailed mean direction versus frequency plots in [Jackson \(1996\)](#) for the individual northern and southern leg radar files on 15 and 16 February shows no obvious current interaction effects for the eastward-traveling waves on the 15th. Significant differences are evident though in the same plots for 16 February for the northern leg files S03–S06 versus the southern leg files S14–S11 at comparable fetches. The southern leg spectra show fairly close alignment with the wind direction at all frequencies, although there is a tendency for clockwise rotation with frequency away from the wind direction (toward the south). The northern leg data on the other hand show a significant counterclockwise rotation away from the wind direction (toward the north) for all frequencies, including frequencies near the peak. The overall mean directions are, in fact, rotated away from the wind direction to the north by about 20° . This can be seen in the “custer”

diagrams in [Jackson \(1996\)](#) and [Jackson and Jensen \(1995\)](#). The strongest effect is seen in the middle of the northern leg, in spectrum S05, where a second mode appears near the peak frequency, but rotated some 60° counterclockwise from the dominant, downwind mode. This behavior of the wave field is consistent with a reflection of the downwind (to approximately 120°) spectral components by the eastward (to 90°) flowing portion of the Gulf Stream. A similar pattern of reflected waves has been observed by [Kudryavtsev et al. \(1995\)](#) for waves attacking the current from the southwest (cf. their “Experiment 6” data and their [Figs. 2–5](#)). The model computations of [Holthuijsen and Tolmen \(1991\)](#) show that the mean directions for a relatively long 230 m (12 s) windsea attacking a linear Gulf Stream segment at 45° incidence may be rotated by 10° or so in the region of reflected waves. Rotation in the opposite direction is seen in the region of transmitted waves on the opposite side of the current axis. These effects are likely to be stronger for the higher wave frequencies involved on 16 February.

3. Analysis

In attempting to analyze this event we are confronted with a wealth of environmental data on a complex wind/wave event in inhomogeneous waters with an exceptionally strong current system. A thorough analysis of this wind/wave event, one that includes all relevant data sources, accounts for wave–current interactions and embraces all three dimensions (i.e., coastwise, normal fetch, and duration coordinates), is beyond our present means, so the scope of the present investigation must therefore be limited. First, we shall neglect to treat wave–current interactions. Second, we shall eliminate the coastwise dimension by considering all data to be simply a function of distance offshore (normal fetch). Third, the wave data sources are to be restricted to the radar data and the data from the two directional wave buoys, Discus-N and Discus-C, and the wind data are to be restricted to the data from five buoys, for reasons discussed previously.

The radar and buoy data locations are shown in an x – t diagram of the event in [Fig. 3](#). Here x is the fetch normal to the coastline at Wallops Island, Virginia, and t is the duration relative to 0000 UTC 15 February, which we take to be the nominal epoch for the wind shift. In the transformation of the data to the coastal coordinate system, we assume a coastline orientation of 28.6° true. The radar data (here shown as circles) inshore of 125 km are omitted in this plot since they are not used in the subsequent analysis. The hourly observations for the four SWADE directional wave buoys are represented in this figure by dashed lines. As mentioned, of these four buoys, only Discus-N (WMO buoy number 44001) and Discus-C (WMO buoy number 44023) will be used in the analysis. The straight lines originating from $(x, t) = (0 \text{ km}, 0 \text{ h})$ are the mean direction propagation characteristics computed according to a nominal advection velocity based on the mean of the radar spreading data for 15 February (see section 3a). The six characteristics are for the six chosen analysis bands between 0.11 and 0.22 Hz. It is seen that relative to the buoys at ca. 100-km fetch, much more of the radar data lie in a duration-limited regime.

For the analysis, the radar mean direction, energy, and directional spreading data are band averaged in the six frequency bands between 0.11 and 0.22 Hz. [Table 1](#) gives the center frequency for each band. Each radar band contains three elementary bands. However, because of correlation overlap, there is no proportional increase in the degrees of freedom for the band average. The 0.01-Hz resolution buoy data are band averaged in 0.03-Hz bands and then evaluated at the radar analysis frequencies using cubic spline interpolation.

a. Relaxation model

Assuming that there are no coastwise wave field gradients and no currents, the wave spectral energy transport equation is

$$dE/dt = \partial E / \partial t + c_g \cos \theta \partial E / \partial x = S, (5)$$

where $E = E(f, \theta; x, t)$ is the directional energy, or height variance spectrum; $c_g = c(f)/2 = g/4\pi f$ is the wave group velocity; $S = S(f, \theta; x, t)$ is the net source function consisting of wind input, dissipation, and nonlinear spectral transfer terms; x and t are the normal fetch and the duration coordinates; and f and θ are, respectively, the wave frequency and the wave direction.

[Equation \(5\)](#) may be transformed into a simple advection equation for mean direction if we assume, for the purpose of closure, that the first and second harmonic phase angles are equal. Examination of the ROWS data shows that this is not an unreasonable assumption to make, at least for the present purpose. In support of this also, we note [Quando and Komen’s \(1993\)](#) finding that the symmetric spreading function approximation that is implied by the equality of the two harmonic phase angles is a reasonable one to make, even in the case of rapidly evolving spectra in turning winds. If we associate the mean direction $\bar{\theta}_f$ with the second harmonic phase angle according to [\(4\)](#), then it follows, on taking the zeroth and first angular harmonic transforms of [\(5\)](#) and invoking the closure hypothesis on the phase angles, that

$$\begin{aligned} & \times \left\{ \frac{\partial \bar{\theta}}{\partial x} - \frac{1}{2} \tan \bar{\theta} \left[(r_2^{-1} - 1) \frac{\partial \ln \mathcal{E}}{\partial x} - \frac{\partial \ln r_2}{\partial x} \right] \right\} \\ & = \mathfrak{S}(Z_{1S}/Z_{1E}). \end{aligned} \quad (6)$$

In (6) the f dependence of $\bar{\theta}$, as well as the other variables, is implicit; $Z_n = \int_0^{2\pi} e^{in\theta}(\cdot) d\theta$, $n = 0, 1, 2$, is the angular transform; $\mathcal{E} = Z_{0E}$ is the nondirectional energy spectrum; and $V_\theta = (r_2/r_1) c_g$ is the mean direction advection velocity, where the r_n , $n = 1, 2$, are the harmonic amplitudes $r_n = |Z_{nE}|/\mathcal{E}$.

We note that in calculating the advection term we will be making the assumption that r_1 and r_2 are functionally related so that only three variables will need to be considered in the analysis. Thus, rather than use the actual radar-measured r_1 , we infer it from the measured r_2 , assuming that the spectrum can be described by a $\cos^{2s}(\theta/2)$ spread law. As mentioned above, [Quando and Komen \(1993\)](#) find that this symmetrical spread law provides a reasonable approximation for the directional spectrum, even in turning wind cases. The dependent variables (observables) we shall be considering in the subsequent analysis are then to be $\bar{\theta}$, \mathcal{E} , and V_θ .

[Holthuijsen et al. \(1987\)](#) observe that the right-hand side of (6) is proportional to the energy growth rate. Indeed, as shown by [Holthuijsen et al. \(1987\)](#) and by [Quando and Komen \(1993\)](#), [Eq. \(6\)](#) can be written in precisely the same form as the directional relaxation model [equations \(1\) and \(3\)](#), the only difference being that the wind direction is now replaced by the mean direction of the source term, or the same, the mean direction of energy growth, namely,

$$d\bar{\theta}_f/dt = \mathfrak{S}(Z_{1S}/Z_{1E}) = (1/\tau_{fS}) \sin(\bar{\theta}_{fS} - \bar{\theta}_f), \quad (7)$$

where $1/\tau_{fS} = (r_{1S}/r_{1E}) d \ln \mathcal{E}/dt$ and $\bar{\theta}_{fS} = \arg(Z_{1S})$. [Quando and Komen \(1993\)](#) emphasize that, while [Eq. \(1\)](#) is an approximation, [Eq. \(7\)](#) is exact. An indication of how (1) may fail to properly model the directional response is given by their finding, from numerical simulations, that $\bar{\theta}_{fS}$ can differ significantly from the wind direction θ_w . It is noteworthy that (7) implies that, for wave turning to occur at all, there must be an accompanying change in the total energy density $\mathcal{E}(f)$ and that this must be positive for waves turning into the direction of energy input.

b. Data synthesis

The analysis approach is to combine the in situ and radar observations of mean direction by least squares fitting a two-dimensional, space–time polynomial surface to the two sets of observations in each of the six analysis frequency bands. [Figure 4](#) shows the raw radar mean direction data and the hourly mean direction data from Discus-N for the six analysis frequency bands that are to be subjected to least squares fit (LSF). The radar data include all radar observations for fetches greater than 125 km. The buoy data include all hourly observations between -6 and $+48$ h relative to 0000 UTC 15 February 1991. The radar data are seen to be rather noisy. The large fluctuations in direction can be attributed to several factors: 1) The observations are not, in fact, spatially contiguous but are made up of observations separated by as much as 100 km in the coastwise direction; 2) the spatially distributed data will necessarily be subject to fluctuations, even for contiguous observations, because of wave interactions with spatially varying currents; and 3) the radar harmonic data at the higher frequencies may be noisy because of low signal to noise background levels and unresolved toggling associated with the 90° ambiguity in the second harmonic estimator.

The mean direction and energy data are fitted with fourth-degree polynomials in fetch and duration. Equal unit weighting is given to each of the 35 radar and 55 buoy data points. In the case of the advection velocity the fit is limited to the second degree with the buoy data excluded. The lower degree fit is necessary because the radar data are very noisy. The buoy V_θ data are excluded from the fit because there is a large mismatch between the radar and buoy spread parameter data [see appendix C]. [Figure 5](#) shows the fitted surfaces for mean direction and energy for the combined radar and Discus-N data case shown in [Fig. 4](#). For reference, the Discus-N time series are shown on the plots. The plot domain in this figure is 0–40 h in duration and 100–300 km in fetch. The fit surface data are here plotted on a 20×20 rectangular grid. This same grid will be used for the finite difference estimation of the local time derivative and advection terms in [Eq. \(6\)](#).

It is seen that the fourth-degree fitted mean direction and energy surfaces match fairly well the buoy time series data around 100-km fetch. [Figure 6](#) gives an example of cuts through the six fitted mean direction surfaces at a given fetch.

The example shows the temporal response curves for the Discus-N data case at a fetch of 195 km. Also shown are the five-buoy vector-averaged wind speed and direction data. In this example, band 1 (0.11 Hz) is seen to exhibit a slight turning away from the wind direction early on in the event. The band 1 mean directions do not start to turn into the new wind direction until fairly late in the event at $t = 15$ h or so. The higher frequencies start to turn into the new wind direction almost immediately following epoch.

c. Parameter estimation

The substantial time derivative of the mean direction in (6) is estimated from the gridded LSF surfaces of mean direction, energy, and advection velocity using simple forward differences. A number of cases can be considered that include different combinations of buoy wind and wave data and analysis fetch. As well, we can vary the fit degree and can either include or exclude the advection term in the analysis. Finally, we have several ways to go about estimating the relaxation parameter from these data. These are:

1) FROM THE E -FOLDING TIMESCALE: THE ESTIMATE B_T

This estimate is useful as a “reality check” for the other estimates. For a steplike change in wind direction at $t = 0$, the solution of (1) is (Hasselmann et al. 1980)

$$\tan[(\bar{\theta}_f - \theta_w)/2] = \tan[(\bar{\theta}_{fi} - \theta_w)/2]e^{-2\pi f b t}, (8)$$

where $\bar{\theta}_{fi}$ is the initial wave direction at $t = 0$ and θ_w is the new wind direction, which is taken to be the wind direction at $t = 40$ h. From the smoothed temporal response data at a given fetch, the relaxation constant b_τ is estimated from the time $t = \tau_f$ at which the observed mean wave direction equals the model solution direction for one e -folding, that is, when $2\pi b f t = 1$.

2) BY THE FINITE-DIFFERENCE METHOD: THE ESTIMATE B_{FD}

This method of estimating b is used by van Vledder and Holthuijsen (1993). For every time step in the event window an estimate of b , $b = b_i$ say, is made by ratioing the time rate of change of mean direction with the factor of b on the right-hand side of (1). The final estimate of b is simply the mean of the individual b_i estimates over the event window. The major problem in estimation, besides the selection of appropriate wind/wave events and the selection of event windows, is deciding whether the data need to be conditioned in any way. van Vledder and Holthuijsen (1993) apply the following constraints to the data:

1. The difference between the mean wave direction and the wind direction should be no greater than 90° and no less than 10° .
2. The wave direction must be turning toward the wind direction. This means that the individual estimates b_i are restricted to nonnegative values $b_i \geq 0$.
3. For an individual estimate b_i to be considered valid, the frequency for the particular estimate must be greater than the directional Pierson–Moskowitz (PM) limit for the given mean wave direction and local wind direction at the given time step; that is, we must have

$$f > f_{PM} \sec(\bar{\theta}_f - \theta_w), (9)$$

where $f_{PM} = 0.13g/U$ is the Pierson–Moskowitz peak frequency for a fully developed sea.

3) BY THE “REGRESSION” METHOD: THE ESTIMATE B_{LSF}

This is the method used by Hasselmann et al. (1980). For the event as a whole, a b value is determined from a one parameter linear regression of $Y = d\bar{\theta}_f/dt$ on $X = 2\pi f \sin(\theta_w - \bar{\theta}_f)$; thus b is given by $b_{LSF} = \Sigma X_i Y_i / \Sigma X_i^2$. The regression may be performed for a fixed frequency or for a fixed wave-age class interval. In the latter case, the moments for a given class of U/c are accumulated when the U/c value at a time step falls within that class interval. Hasselmann et al. (1980) grouped their b estimates in three inverse wave-age classes between $U/c = 1.0$ and $U/c = 2.0$. These class intervals are defined in Table 2. Hasselmann et al. (1980) did not apply constraints to their data; however, constraints were applied in

d. Case generation

While the basic analysis approach has been decided upon, there are yet a number of options available to us in the analysis. These involve the particular choice of the buoy wind and wave data to be used (e.g., Discus-N versus Discus-C wave data), various parameter settings, and the parameter estimation method to be used. We will use the statistics of a total of 12 cases to arrive at a set of final estimates of the relaxation parameter. These cases are all based on a fourth-degree polynomial LSF of the combined radar and buoy data as described in [section 3b](#). The 12 cases are manufactured from three equally spaced fetch cuts at $x = 142$ km, 195 km, and 247 km and from the four combinations of buoy input wind and wave data, namely, for Discus-N or Discus-C wave data and for Discus-E winds or the five-buoy average winds. The 12 cases are run both with and without the three constraint conditions enumerated in [section 3c](#).

4. Results

a. Example case results

[Figure 7](#) shows the relaxation model solution [\(8\)](#) for the step-function wind shift compared to the smoothed mean direction data of [Fig. 6](#). From this figure it is seen that only the higher frequency bands are well modeled by [\(8\)](#). The wave response is very different from the model response for the lowest frequency bands. This suggests that the relaxation model with a constant b may not, in general, be adequate for modeling the directional response and that, in practice, the “constant” b may vary with time. [Figure 8](#) shows the temporal evolution of the differential b_i estimates for the unconstrained and constrained data cases A2 and B2 (five-buoy average winds; 195-km fetch). In the unconstrained case the data span the event window. All estimates except bands 1 and 2 are seen to peak in mid event. Peak values of b_i of over 10×10^{-5} are seen for band 4. Of all bands, only band 6 (0.22 Hz) appears as fairly constant with time across the event window. Band 1 (0.11 Hz) exhibits a monotonically increasing behavior with duration, reaching a maximum of $b_i \sim 10 \times 10^{-5}$ at the end of the event. In the constrained data case, bands 2–6 are confined to mid event and their peak values are limited. Bands 1 and 2 have only a few data points that survive the constraint filter, and these are at the end of the event. Band 1 has only two data points left with values around 10×10^{-5} . Band 1 data in the first 20 hours fail to meet criteria 1 and 2 in [section 3c](#). All band 1 data save the few points at the end of the event fail to pass criterion 3, the Pierson–Moskowitz directional limit.

[Figures 9](#) and [10](#) show the results of the relaxation parameter estimation for the example data case (Discus-N wave data; five-buoy average winds; 195 km-fetch). In [Fig. 9](#), no constraints are applied to the mean direction data. Without the advection correction, the finite difference and regression estimates are fairly close to the e -folding estimates, which are nearly constant across the bands with values around 1.5×10^{-5} . The advection correction raises the values of the finite difference and regression estimates by 25%–50%. Values of b around 3×10^{-5} are seen for intermediate wave ages, $U/c \sim 1.5$. For lower frequencies the b values are comparable; for the higher frequencies and U/c values, the mean b estimates are appreciably lower, with $b \sim 1.5 \times 10^{-5}$. [Figure 10](#) shows the same estimates, but for the constrained data case. For the intermediate wave ages the application of the constraints has little effect. The higher U/c estimates are raised to a level more on par with the intermediate wave age values. In the lowest range, $U/c \sim 1$, the estimates are 2–3 times the values in the unconstrained case. These high values are due entirely to the few band 1 data points at the end of the event.

[Tables 1](#) and [2](#) list these example results along with other relevant statistics. [Table 1](#) list the finite difference results b_{FD} . The following are given for each of the six analysis frequency bands: the band center frequency, the LSF standard deviation for the mean direction σ_θ , the mean inverse wave age $\langle U/c \rangle$, the e -folding relaxation parameter estimate b_e , and the mean estimates b_{tFD} and b_{FD} for the local time derivative only and advection-corrected cases, respectively. The fit error σ_θ is seen to be around 15° for all bands but band 6, where it is $\sim 21^\circ$. [Table 2](#) shows regression results b_{LSF} versus U/c class for the same example case. The results are given along with the standard deviations and correlation coefficients for the regressions.

b. Summary of case results

[Figure 11](#) summarizes the results for the regression estimates b_{LSF} for the 12 individual cases consisting of the various combinations of buoy wave and wind input data and analysis fetch as described in [section 3d](#). The figure shows the results for the three U/c classes plotted versus the analysis fetch. It is seen that the class 2 estimates lie intermediate between the (higher) class 1 and (lower) class 3 estimates; that the estimates for the three wave age classes converge with increasing

fetch. At the longest fetch, 247 km, the average estimate for all wave age classes is $b_{\text{LSF}} = 2.9(\pm 0.14) \times 10^{-5}$. As

discussed, the class 1 estimates for the shorter analysis fetches (142 and 195 km) are very high because of the anomalous (nonmodel) behavior of the lowest frequency band (0.11 Hz). The class 3 estimates, particularly for the shorter fetches, are significantly lower ($\sim 50\%$) than the class two estimates. This may be due to oversmoothing of band 5 and 6 data; also we note that the radar data for these bands are relatively noisy, and thus these estimates are relatively unreliable. For wave age class 2 ($1.2 \lesssim U/c < 1.6$), the most populous and reliable wave age class, the average for all cases, including all fetches is

$$b_{\text{LSF}} = 3.3(\pm 0.14) \times 10^{-5}. \quad (10)$$

Basically similar results are found for the finite difference estimates b_{FD} . These estimates are about 10% higher than the regression estimates shown in [Fig. 11](#). For U/c class 2, $b_{\text{FD}} = 3.8 \times 10^{-5}$. In general, we find on examining the behavior of the estimates for all cases run both with and without constraint conditions and advection corrections that the regression estimates are more consistent in the sense that they exhibit significantly less case-to-case variability than the finite difference estimates. We thus tend to give more credence to the regression results.

Another way of viewing the data is via a one parameter regression for the lumped data of all individual cases. We perform this regression for the 12 data cases with and without advection correction and with and without constraint conditions. The matrix of results is given in [Table 3](#). The results are virtually identical to the mean of the individual case regression results. Correlation coefficients ρ are given in the table for both one and two parameter linear regressions. For the one parameter regression, $\rho_1 = (\Sigma X^2 / \Sigma Y^2)^{1/2} b_{\text{LSF}}$. The correlation coefficients ρ_2 for standard two parameter regressions are rather low. For the lumped data regression corresponding to the wave age class 2 result [\(10\)](#) above, $\rho_2 = 0.30$. The correlation coefficients for the individual cases can be much higher, but sometimes they are lower. We see that the advection correction increases the correlation only in the unconstrained data case; in the constrained case it is slightly reduced. In both cases the advection correction slightly increases the standard deviations.

5. Discussion

Examination of several wind turning events reported in the literature shows the wind/wave event here to be fairly typical. If anything, the conditions of the present study are better than average. There is no swell (i.e., apart from the fact that the initial windsea may technically be called swell), and the wind speed variability is less than in a number of published studies. What is atypical here is the offshore wind situation and the presence of a strong current system (Gulf Stream). Wave refraction by the current may affect the results by 1) making the spatially distributed radar data noisier than they might be otherwise, and 2) by introducing biases in mean wave directions. As discussed in [section 2c](#), wave refraction effects are most pronounced in the beginning of the event for the northward-directed system near shore (creation of wave shadow region and possibly caustics) and toward the end of the event for the fetch-limited waves on the north side of the eastward flowing portion of the current (creation of reflected wave system). The extreme wave field variability near the shelf break on 14 February caused by refraction may result in some mismatching of buoy and radar data at the inner edge of the analysis region near 100-km fetch. On the 16th, reflected waves may be rotating the mean directions on the northern flight leg away from the wind direction by as much as 30° . The southern leg data tend to rotate in the opposite direction with increasing frequency. The contrary rotations are responsible for the “jitter” seen in the radar mean direction data for this flight in [Fig. 4](#). Although the contrary rotations tend to cancel each other on average, there may yet be some biasing of the mean direction data away from the new wind direction toward the initial wind direction. This would have the effect of biasing the relaxation constant estimates on the low side. To see what the magnitude of the effect might be we consider constraining the radar data of the last flight so that the mean directions for all frequencies are identically equal to the wind direction. Subject to this constraint, the results for the case B2 (cf. [Table 2](#)) is $b_{\text{LSF}} = (7.0, 4.2, 2.5) \times 10^{-5}$ for the three U/c classes. It is thus quite possible that our estimate of b [[Eq. \(10\)](#)] is biased low by as much as 20%.

The fetch-limited situation that occurs in the middle and late stages of the wind/wave event has been dealt with by modeling advection using the spatially distributed radar data in a one-dimensional advection equation [[Eq. \(6\)](#)]. The results are somewhat disappointing. The estimates of the relaxation parameter without the advection correction generally appear to be better behaved in that they exhibit less variability between U/c classes and versus fetch. The exception is for long fetch, $x = 247$ km, where the individual case estimates actually exhibit significantly less variability. Part of the problem may lie in spurious curvatures of the fit surfaces in the fetch dimension resulting from noisy radar data and data matching problems at the inner 100-km fetch boundary. However, we note that a similar increase in the variability of relaxation parameter estimates was found in the case of the advection corrected data in the [van Vledder and Holthuijsen \(1993\)](#) study using model wave data. The lower-frequency bands are most affected by the correction, as might be expected. The effect is then exaggerated when constraint conditions are added. The first two fetches have very high U/c class 1 values for the advection corrected and constrained estimates compared to the class 2 and 3 estimates.

The apparent biasing of the low-frequency, advection-corrected data, particularly at short fetch, is mainly due to the Pierson–Moskowitz directional limit constraint 3. While constraints 1 and 2 cause low-frequency data early on in the event to be rejected, constraint 3 results in data rejection in much of the ensuing time after wave turning has been initiated. This leaves only a few data remaining at the end of the event, and these data have very high b values (cf. [Fig. 8b](#)). The relaxation model is clearly not adequate for modeling the lowest frequencies, particularly at shorter fetches. The directional response at the lowest two frequencies is very much delayed relative to the wind shift and the response at the higher frequencies. A change of the mean direction does not occur until the new windsea at approximately 90° to the initial sea has grown to the point where it possesses significant energy at a frequency equal to the analysis frequency [see [Jackson and Jensen \(1995\)](#) for examples of the bimodal spectra on 15 February]. In the case of the buoy data, there is an abrupt shift in the mean direction around the time this occurs; this can be seen in the buoy record traces in [Fig. 4](#). The practical implication of this is that in analyzing the response for the directional relaxation parameter by finite differences, one cannot ignore the “dead time” before the mean wave direction starts to turn without getting unrealistic estimates of the wave directional response timescale. For example, the differential b_1 during this dead time may be noisy and frequently negative, and thus if they are rejected by criterion 2 in [section 3c](#) this will result in a positively biased estimate of b . A better estimate of the relaxation timescale in this case would simply be the time elapsed before the abrupt shift, or the same, the timescale for the development of the new windsea.

Because of the data smoothing in the LSF (least squares fit), the data are not noisy in a way that might produce negative b values. The negative b values come about—mostly late in the event—as an artifact of the curve fitting. Thus, this constraint does not have a high impact on the estimates of this study. If, however, the same methodology is applied to the hourly buoy time series, the non-negativity requirement can produce very biased results. [Figure 12](#) shows the estimates of b_t derived from Discus-N data alone, with and without the requirement that $\partial\bar{\theta}/\partial t$ be negative—or the same—that b_t be positive. For both finite difference and regression estimates, the positivity constraint causes the estimates to be biased high by as much as a factor of 2.

a. Comparison with other data

[Table 4](#) lists the results of the present study among the several study results summarized by [van Vledder and Holthuijsen \(1993\)](#) in their [Table 3](#). These results include both field study results and numerical model simulation results and include both b values and χ values from the [Gunther et al. \(1981\)](#) relaxation model (3). We note that the band 1 (0.11 Hz) mean direction in our study has almost the same response as the overall mean direction θ_o (in our case, an energy weighted rather than momentum weighted mean direction). Thus, if we assume as a nominal value of b our wave age class 2 estimate $b = 3.3 \times 10^{-5}$ and assume that this value holds for the lower frequencies and, in particular, for the fully developed peak frequency $f = f_{PM}$, then it follows from (1) and (3) that $\chi = 0.16 \times 10^{-2}$.

In [Table 4](#) we have included the number of distinct wind/wave events involved in each study, as this provides an indication of the weight to be accorded each estimate, all other factors being equal. It is seen that the number of actual wind turning events is quite small. The present estimate (10) is seen to be closest to [Masson’s \(1990\)](#) regression result. The [Hasselmann et al. \(1980\)](#) and [Allender et al. \(1983\)](#) data are seen to be close to our unconstrained results in [Table 3](#). The [Holthuijsen et al. \(1987\)](#) and [van Vledder and Holthuijsen \(1993\)](#) data, including their results from their reanalysis of the Allender et al. (1980) data, are rather high compared to other results in [Table 4](#). We are not sure why. However, we note that use of the constraints may in certain instances introduce positive bias. As discussed, this can happen when the positivity requirement is applied to noisy time series data. [Quando and Komen \(1993\)](#) reanalyzed the [Holthuijsen et al. \(1987\)](#) original data according to an approximation to (7) and found significantly smaller values that were in much better agreement with the results of the EXACT-NL model. Also, [Masson \(1990\)](#) found lower χ values in her reanalysis of van Vledder and Holthuijsen data. We note that while the EXACT-NL model results of [Young et al. \(1987\)](#) shown in [Table 4](#) for moderate U/c are close to the present results, the model results give much shorter timescales for higher U/c values than are indicated by the field data. For example, the [Young et al. \(1987\)](#) result for a 60° wind shift is $b = 4.2 \times 10^{-5}$ for $U/c = 1.6$, while for $U/c = 2.2$ it is $b = 10 \times 10^{-5}$.

6. Conclusions

The study here of a single, well-documented wind-turning event has led to estimates of the wave directional relaxation parameter b that are consistent with most of the published field study estimates and with model simulation results for moderate values of inverse wave age U/c . For the most reliable and well-populated wave age class in our study, $1.2 \leq U/c < 1.6$, we find $b = 3.3 \times 10^{-5}$.

In the case of a large, $\sim 90^\circ$ wind shift, the directional response for frequencies near the spectral peak is not well modeled

by the relaxation model, Eq. (1). The response for the lowest-frequency bands is closer to a step function than it is to a continuous relaxation (cf. the buoy traces in Fig. 4). While the overall, integral timescale for the low frequencies accords with the frequency scaling of the relaxation model, the timescale based on the differential estimates of the relaxation parameter can depart radically from this frequency scaling. On the other hand, the response data for the highest-frequency bands in this study (0.19 and 0.22 Hz) may be unreliable because of low signal-to-noise in the radar data, and because of oversmoothing of these data.

The presence of the Gulf Stream in the experiment area adversely affected this study in several ways. Data from a centrally located buoy, Discus-E, had to be discarded because of direct interaction with the current. Wave refraction was significant, particularly during the initial and final phases of the wind/wave event. Reflected waves during final phase of the event may be biasing the present estimate of the relaxation parameter on the low side by as much as 20%. Thus, it is quite possible that the “true” value of b is closer to 4×10^{-5} .

The radar data in this study permitted advection effects to be addressed. In general, we found that the advection of mean direction added to the total turning rate and increased the values of the relaxation constant estimates. But we also found that the advection term tended to increase the variability of the estimates. Part of the problem may be that the data are simply too noisy (in large part as a result of wave–current interactions). At the shorter fetches, statistical mismatching of radar and buoy datasets and large wave field variability (again, as a result of wave–current interactions) may be adversely affecting the results. The most consistent results were found for the longest analysis fetch (247 km) where advection is smallest.

The availability today of high-resolution directional spectrum data from remote sensing instruments like the Radar Ocean Wave Spectrometer should prompt a rethinking of the directional relaxation problem. While the model (1) seems to be a reasonable approximation for moderate to high U/c values and for small to moderate wind shifts, it may fail otherwise to adequately represent the wave response, and in these cases estimates of the directional relaxation parameter will be of little use in assessing wave model performance or in elucidating the physics involved. The formulation of the directional relaxation in terms of the identity (7) may prove helpful in this respect.

Acknowledgments

The radar data in this study were collected by the first author (FCJ) when he was with NASA’s Goddard Space Flight Center. Funding for the data collection was provided by NASA and by the U.S. Army Corps of Engineers (USACE). FCJ’s contribution to the present work was made under Contract DACA39-96-M-1885 to USACE (USAEWES). REJ conducted his portion of the work at the Coastal Engineering Research Center of USAEWES under the Coastal Research and Development Program, “Upgrading of Discrete Spectral Wave Modelling Work Unit.” Permission was granted by Headquarters, U.S. Army Corps of Engineers, to publish this information. We thank two anonymous reviewers for their helpful comments.

REFERENCES

- Allender, J. H., J. Albrecht, and G. Hamilton, 1983: Observations of directional relaxation of wind sea spectra. *J. Phys. Oceanogr.*, **13**, 1519–1524. [Find this article online](#)
- Caruso, M. J., H. C. Graber, R. E. Jensen, and M. A. Donelan, 1994: Observations and modelling of winds and waves during the Surface Wave Dynamics Experiment, Report 2: Intensive Observation Period IOP-3, 25 February–9 March, 1991. Tech. Rep. CERC-93-6, U.S. Army Corps of Engineers Waterways Experiment Station, Vicksburg, MS, 294 pp. [Available from U.S. Army Corps of Engineers, Waterways Experiment Station, Vicksburg, MS 39180.]
- Donelan, M. A., J. Hamilton, and W. H. Hui, 1985: Directional spectra of wind-generated waves. *Philos. Trans. Roy. Soc. London, Ser. A*, **315**, 509–562.
- Gunther, H., W. Rosenthal, and M. Dunkel, 1981: The response of surface gravity waves to changing wind direction. *J. Phys. Oceanogr.*, **11**, 718–728. [Find this article online](#)
- Hasselmann, D. E., M. Dunkel, and J. A. Ewing, 1980: Directional wave spectra observed during JONSWAP 1973. *J. Phys. Oceanogr.*, **10**, 1264–1280. [Find this article online](#)
- Holthuijsen, L. H., and H. L. Tolman, 1991: Effects of the Gulf Stream on ocean waves. *J. Geophys. Res.*, **96** (C7), 12 755–12 771.
- , A. J. Kuik, and E. Mosselman, 1987: The response of wave directions to changing wind directions. *J. Phys. Oceanogr.*, **17**, 845–853. [Find this article online](#)

Jackson, F. C., 1981: An analysis of short pulse and dual frequency techniques for measuring ocean wave spectra from satellites. *Radio Sci.*, **16**, 1385–400..

—, 1991: Directional spectra from the Radar Ocean Wave Spectrometer during LEWEX. *Directional Ocean Wave Spectra*, R. Beal, Ed., The Johns Hopkins University Press, 91–97..

—, 1996: Observations and modelling of winds and waves during the Surface Wave Dynamics Experiment, Rep. 4: ROWS wind and wave observations, 12 February–7 March, 1991. Tech. Rep. CERC-93-6, U.S. Army Corps of Engineers Waterways Experiment Station, Vicksburg, MS, 245 pp. [Available from U.S. Army Corps of Engineers, Waterways Experiment Station, Vicksburg, MS 39180].

—, and R. E. Jensen, 1995: Wave field response to frontal passages during SWADE. *J. Coastal Res.*, **11**, 34–67..

—, W. T. Walton, and C. Y. Peng, 1985a: A comparison between in situ and airborne radar observations of ocean wave directionality. *J. Geophys. Res.*, **90** (C1), 1005–1018..

—, —, and P. L. Baker, 1985b: Aircraft and satellite measurement of ocean wave directional spectra using scanning beam microwave radars. *J. Geophys. Res.*, **90** (C1), 987–1004..

Kudryavtsev, V. N., S. A. Grodsky, V. A. Dulov, and A. N. Bol'shakov, 1995: Observations of wind waves in the Gulf Stream frontal zone. *J. Geophys. Res.*, **100** (C10), 20 715–20 727..

Large, W., and S. Pond, 1981: Open ocean momentum flux measurements in moderate to strong winds. *J. Phys. Oceanogr.*, **11**, 324–336.. [Find this article online](#)

Liu, A. K., F. C. Jackson, E. J. Walsh, and C. Y. Peng, 1989: A case study of wave–current interaction near an oceanic front. *J. Geophys. Res.*, **94** (C11), 16 189–16 200..

Masson, D., 1990: Observations of the response of sea waves to veering winds. *J. Phys. Oceanogr.*, **20**, 1876–1885.. [Find this article online](#)

Oberholtzer, D., and M. Donelan, 1996: SWADE data guide. NASA Ref. Pub. 1338, NASA Goddard Space Flight Center., Greenbelt, MD, 108 pp. [Available from NASA/Goddard Space Flight Center, Greenbelt, MD 20771].

Quando, G., and G. Komen, 1993: Directional response of ocean waves to changing wind direction. *J. Phys. Oceanogr.*, **23**, 1561–1565.. [Find this article online](#)

Shay, L. K., P. C. Zhang, H. C. Graber, and E. J. Walsh, 1996: Simulated surface wave current interactions during SWADE. *Global Atmos. Ocean Sys.*, **5**, 125–150..

Van Vledder, G. Ph., and L.H. Holthuijsen, 1987: Waves in turning wind fields. *Proc. 21st Coastal Engineering Conf.*, Malaga, Spain, ASCE, 602–611..

—, and —, 1993: The directional response of ocean waves to turning winds. *J. Phys. Oceanogr.*, **23**, 177–192.. [Find this article online](#)

Walsh, E. J., D. W. Hancock III, D. E. Hines, R. N. Swift, and J. F. Scott, 1985: Directional wave spectra measured with the surface contour radar. *J. Phys. Oceanogr.*, **15**, 566–592.. [Find this article online](#)

—, L. K. Shay, H. C. Graber, A. Guillaume, D. Vandemark, D. E. Hines, R. N. Swift, and J. F. Scott, 1996: Observations of surface wave–current interaction during SWADE. *Global Atmos. Ocean Sys.*, **5**, 99–124..

WAMDI Group, 1988: The WAM model—A third generation ocean wave prediction model. *J. Phys. Oceanogr.*, **18**, 1775–1810.. [Find this article online](#)

Weller, R. A., M. A. Donelan, M. G. Briscoe, and N. E. Huang, 1991: Riding the crest: A tale of two wave experiments. *Bull. Amer. Meteor. Soc.*, **72**, 163–183.. [Find this article online](#)

Young, I. R., S. Hasselmann, and K. Hasselmann, 1987: Computations of the response of a wave spectrum to a sudden change in wind direction. *J. Phys. Oceanogr.*, **17**, 1317–1338.. [Find this article online](#)

APPENDIX A

7. Discus-E Data

Wave data from Discus-E appear to be corrupted by the buoy's physical contact with the Gulf Stream. Although the current data shown in [Fig. 1](#) indicate that there is only a small current at the stream margin where Discus-E is located, the wave data from the indicate that there is only a small current at the stream margin where Discus-E is located, the wave data from the buoy itself indicate a significant effect. [Figures A1](#) and [A2](#) compare buoy data on 15 February with radar data at the same fetch. In the directional spectrum comparison of [Fig. A1](#), one sees that the developing, eastward-traveling, windsea mode in the radar spectrum has a frequency of about 0.14 Hz, whereas the modal frequency for the buoy is around 0.18 Hz. The radar-observed frequency is consistent with the development of this mode with fetch; the buoy-observed frequency is not. The inconsistency is obvious in the buoy spectrum plots of Fig. 16 in [Jackson and Jensen \(1995\)](#). These spectra show both Discus-N and Discus-C, at a fetch of about 100 km, to have peak frequencies for this mode of 0.16–0.17 Hz, whereas Discus-E, at nearly twice the fetch, records a significantly higher frequency ~ 0.2 Hz. One expects there to be a frequency downshifting of the windsea with fetch x that scales roughly as $x^{-1/3}$ (e.g., cf. [Jackson and Jensen 1995](#)). Indeed, the radar-observed frequency of 0.14 Hz scales accordingly. Further evidence of a data problem with Discus-E can be seen in [Fig. A2](#), which compares the radar and buoy nondirectional energy spectra. It is seen that the radar data follow the expected f^{-4} power-law dependence for the rear face region of the windsea spectrum,

$$\mathcal{E}(f) = (2\pi)^{-4} \alpha_U U g f^{-4}, \quad (\text{A1})$$

where $\alpha_U = 0.025$ and where here U is taken to be the buoy observed neutral wind speed of 11.8 m s^{-1} . The buoy data, on the other hand, show a marked deviation from this power law. Doppler shifting alone cannot account for this large effect since the current speed would have to around 3 m s^{-1} to explain the modal frequency shift of ~ 0.04 Hz seen in [Fig. A1](#). Although the current is larger at Discus-E than indicated in the maps of [Fig. 1](#) (because of a slight misregistration of the data fields), this current speed is still quite high; possibly, dynamic loading effects are also responsible for the behavior of the Discus-E data.

APPENDIX B

8. Radar Data

The radar data for short fetches ($x < 125$ km) have been rejected in this study because many of these spectra are of relatively poor quality compared to the spectra at longer fetches. Generally, ROWS is not recommended for windseas with significant wave heights less than 2 m ([Jackson et al. 1985b](#)) because the relatively low level of signal power can result in poor spectrum definition under these conditions. Both residual background fading (speckle) noise and leakage of “dc” power conspire to contaminate these spectra. The dc power arises from antenna pattern (finite data window) effects and from antenna beam motions (from aircraft pitching and rolling) that make it difficult to properly normalize the signal. In SWADE the signal was normalized with a model function for the average backscattered power based on a skewed normal distribution of specular wave slopes. This procedure allowed more low-frequency, or dc, power to affect the spectra than would have been the case had we used a more fully adaptive signal power normalization routine as in some previous missions (e.g., [Jackson 1991](#)). In addition, we may expect some low-frequency power to be generated as intermodulation products in the basic microwave scattering process ([Jackson 1981](#)).

[Figure B1](#) is a log–log plot of all the (fetch limited) radar energy spectra for 16 February. In these spectra, the low-frequency, or dc, energy content is apparent for frequencies below 0.1 Hz. One also sees a roll-off in power above 0.2 Hz (40-m wavelength). This high-frequency signal attenuation can be attributed to an imperfect point target response (PTR) correction. However, intrinsic scattering effects may also be contributing to this roll-off in power (cf. [Jackson 1981](#); [Jackson et al. 1985b](#)). In the wave-energy containing part of the radar spectrum, between ca. 0.1 and 0.2 Hz, we see that the envelope of peak energy densities follows the Phillips law, $\mathcal{E}(f) = (2\pi)^{-4} \beta g^2 f^{-5}$, where the Phillips constant $\beta = 8.1 \times 10^{-3}$.

In the present analysis we have rejected all the radar spectra for fetches $x < 125$ km. While many of these low-energy spectra could have been used in the present analysis (e.g., see the radar–buoy comparison in [Figs. B2–B4](#)), we have decided, for convenience, to eliminate all these spectra. This is not a great loss since (i) the analysis was intended in the first place to concentrate on the longer fetches where advective effects are presumably smaller, (ii) the shelf region data for 14 and 15 February are unreliable because of wave refraction, as discussed, and (iii) the buoy data suffice to define the conditions at the inshore boundary of the analysis domain ($x = 100$ km).

With higher sea states, there still can be problems with signal-to-noise and signal fidelity at the higher frequencies. In the present analysis for mean directions, a noise background template was constructed for each radar spectrum based on the observed spectral power directional minima versus frequency. This procedure produces directional spectra with fairly clean

directional distributions and comparatively narrow spreading (see below); however, these spectra appear to have a deficit in total energy, which is particularly noticeable in the low-energy windsea spectra (wave heights <2 m). For the spectra shown here we have used a slightly modified version of the original fading noise background subtraction given in [Jackson et al. \(1985b\)](#).

APPENDIX C

9. Directional spreading

The text states that there is a considerable discrepancy between the radar- and buoy-derived spread parameter values. This does not mean that there is necessarily a fundamental disagreement between the two measurement systems. On the contrary, we see here that, despite the apparent discrepancy in the spread parameters, the two systems are actually in fairly good agreement. The spread parameter $s = s(f)$ is defined by the standard cosine-power model of the directional spreading function, namely,

$$D(f, \theta) = D_0(s) \cos^{2s}[(\theta - \bar{\theta}_p)/2], \quad (\text{C1})$$

where D_0 is a normalization constant defined so that the directional spectrum $E(f, \theta) = \mathbf{E}(f) D(f, \theta)$. According to the classical method of pitch-roll buoy analysis of Longuet-Higgins, Cartwright and Smith (LHCS), two s values, s_1 and s_2 , are derived by equating the first and second harmonics of the model distribution (C1) to the observed first and second harmonics (e.g., [Hasselmann et al. 1980](#); [Jackson et al. 1985a](#)). In the case of the buoy data, the five angular harmonic coefficients are derived from the auto- and cross-spectra of heave, pitch, and roll motions. These represent essentially all the information in the measurement at any frequency. In the case of the radar data, we derive the harmonics from the actual, observed directional distributions. The first five harmonics thus represent only one sixth of the information available from the 15 direction bands. The buoy would appear to be inherently of much lower directional resolution than the radar; yet, the s_2 values from the buoy are consistently higher than the radar values. In general, for a pitch-roll buoy, s_2 is observed to scatter high relative to s_1 (e.g., [Hasselmann et al. 1980](#)), whereas in the case of direct observations of the directional distribution, the computed s_1 and s_2 are observed to be very nearly equal ([Walsh et al. 1985](#); [Jackson et al. 1985a](#)). At the same time, both s_1 and s_2 values from the radar may appear to be rather low because of 1) background noise and/or 2) because of a real deviation of the actual directional distribution from the model form (C1).

This is illustrated in [Figs. B2–B4](#). [Figure B2](#) compares the radar directional spectrum S22 on 16 February with nearby Discus-N data, where the buoy directional spectrum is here produced by the maximum likelihood method ([Caruso et al. 1994](#)). It is seen that there is, overall, rather good agreement between the two spectra. The radar peak is a little narrower than the buoy peak; at the same time, the radar spectrum has a broader background than the buoy spectrum. [Figure B3](#) compares the radar and buoy MLM directional distributions for the respective peak frequencies (each being ~ 0.13 Hz). Also shown are the model distribution functions (C1) derived from the second harmonics of each of these distributions. The radar derived $s_2 = 6.8$ and the buoy s_2 derived from the MLM directional distribution is $s_2 = 5.0$. It is seen that in both cases, the “fitted” model function (C1) fails to reproduce the sharpness of the spectral peaks. The actual half-power spread of the radar data is about 35° , whereas the corresponding model function half-power spread is about 60° . Interestingly, the buoy $s_2 = 24.1$, derived from the NDBC harmonic coefficient data, gives about the same half-power width as the radar distribution. However, the model distribution with this s_2 value fails to account for the energy in the distribution wings that is a feature of both the radar and buoy MLM spectra.

For reference, we show in [Fig. B3](#) two published spreading function results. Based on first harmonic pitch-roll buoy data, [Hasselmann et al. \(1980\)](#) find for $f \geq f_m$ ($f_m =$ peak frequency) and $c_m/U \leq 1$,

$$\begin{aligned} s_1 &= 9.77(f_m/f)^\mu, \\ \mu &= 2.33 + 1.45(U/c_m - 1.17). \end{aligned} \quad (\text{C2})$$

[Donelan et al. \(1985\)](#) propose a different model spreading function based on wave gauge array data. For $f \geq 0.95 f_m$,

$$\beta = 2.28(f_m/f)^{1.3}. \quad (C3)$$

These two spreading results for $f = f_m$ are plotted in the directional half-space occupied by the radar's symmetrical artifact spectrum. The Hasselmann et al. result (C2) provides a reasonable fit to the radar data (and buoy data as well); the Donelan et al. result (C3) fits the radar data remarkably well.

Figure B4 compares the radar and buoy nondirectional spectra $\mathcal{E}(f)$ and spread parameter estimates $s(f)$ for the same example spectra. In the case of the buoy data, s -parameter estimates are shown as derived from the MLM spectrum and from the archived NDBC data according to the LHCS method. The nondirectional spectra are seen to agree quite well, apart from the radar's excess of low-frequency energy. Both radar and buoy spectra follow the f^{-4} law according to (A1) for $f > 0.15$ Hz. Both the NDBC s_1 and s_2 values are seen to be consistently higher than either of the radar or MLM s_2 values. The Hasselmann et al. spreading model (C2) lies intermediate between these two sets of data. The MLM spread data are peculiar in that they do not show any broadening on the high side of the peak. In contrast, the radar spreading increases rapidly in the rear face region of the spectrum.

Tables

Table 1. Finite-difference estimates for case B2 fit with Discus-N data: fit degree = 2/4, * fetch = 195 km, all constraints, and vector average wind.

	Band number					
	1	2	3	4	5	6
Center frequency (Hz)	0.109	0.128	0.145	0.167	0.192	0.215
R _r error (deg)	14.8	13.7	14.4	14.4	16.7	20.7
Number of points for b/b estimates	27	34	11/11	10/9	9/9	9/9
Mean U/c (for b estimates)	1.1	1.3	1.5	1.4	1.5	1.7
b -folding estimate k^{**}	1.4	1.3	1.5	1.6	1.4	1.3
Mean finite difference b_{10}	6.9	2.6	2.4	2.7	4.9	1.6
Mean finite difference b_{20}	9.2	5.1	3.8	4.8	4.9	2.4

* Degree = 2 is for advection velocity; degree = 4 is for mean direction and energy.
 ** k is arbitrary, $k = 10$.

Click on thumbnail for full-sized image.

Table 2. Regression estimates for case B2 fit with DN data: degree = 2/4, fetch = 195 km, all constraints, and vector average wind.

U/c class ^a	1	2	3
Number of points ^b	7/7	29/28	10/9
Mean U/c	1.11	1.41	1.72
b_{LSF}	3.66	2.72	1.73
\hat{b}_{LSF}	6.04	3.50	2.24
$\sigma_{b/c}$ ^c	0.50	0.27	0.22
ρ_1 ^d	0.98	0.93	0.96
ρ_2 ^d	0.32	0.56	0.70

^a Class 1: $1.0 \leq U/c < 1.2$; Class 2: $1.2 \leq U/c < 1.6$; Class 3: $1.6 \leq U/c \leq 2.0$.
^b Number of data points for b/b .
^c Standard deviation of b_{LSF} .
^d Correlation coefficients for one and two parameter regressions.

Click on thumbnail for full-sized image.

Table 3. Lumped data regressions—All cases.

	Unconstrained cases U/c class			Constrained cases U/c class		
	1	2	3	1	2	3
Number of points	258	432	276	55	267	168
b_{LSF}	1.86	2.07	1.19	5.53	2.64	2.01
\hat{b}_{LSF}	0.09	0.06	0.10	0.20	0.07	0.08
$\sigma_{b/c}$	0.78	0.86	0.58	0.92	0.91	0.88
ρ_1	—	—	0.36	0.20	0.37	0.36
ρ_2	-0.32	0.19	—	—	—	—
Number of points	258	432	276	44	188	108
b_{LSF}	2.96	2.65	1.09	4.81	3.30	2.20
\hat{b}_{LSF}	0.16	0.09	0.11	0.28	0.13	0.10
$\sigma_{b/c}$	0.76	0.81	0.53	0.93	0.91	0.90
ρ_1	-0.19	0.30	—	0.17	0.36	0.33
ρ_2	—	—	—	—	—	—

Click on thumbnail for full-sized image.

Table 4. Relaxation parameter estimates (b and χ values) from various studies (Adapted from van Vledder and Holthuijzen 1993).

Study	U/c range	b ($\times 10^3$)	χ ($\times 10^3$)	Number of events/estimates
Hasselmann et al. (1982)	1.2-1.6	2.8 ± 0.5	—	57
Sumner et al. (1981)	1.1-1.6	—	0.21	34
Altner et al. (1983)	1.1-1.6	1.7	—	1167
Young et al. (1987)	1.6	4.2	—	22
ENACTS Model	2.2	10.0	—	22
Holthuijzen et al. (1987)	0.8-3.1	—	0.41	88
Mason (1993)	1.0-2.0	3.1 ± 0.3	0.12	245
—	1.2-1.6	3.8 ± 0.4	—	245
—	—	—	(0.17)	1212
—	—	—	—	—
van Vledder and Holthuijzen (1988)	1.1-1.7	—	0.57	334
—	—	—	—	—
—	—	(3.4)	—	3180
—	—	(6.5)	—	342
—	—	(6.0)	—	342
—	—	—	—	—
—	—	(8.1)	—	1167
—	—	(10.0)	—	127
—	—	(12.1)	—	127
—	—	—	—	—
—	1.1-1.7	—	0.16	—
Present study	1.2-1.6	2.7 ± 0.1	—	1432
Regression, no constraints	1.2-1.6	3.3 ± 0.1	—	1188
Regression w/ constraints	1.2-1.6	3.8 ± 0.2	—	1188
Inferred χ value	0.8	—	(0.16)	—

Click on thumbnail for full-sized image.

Figures



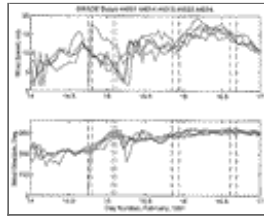
[Click on thumbnail for full-sized image.](#)

Fig. 1. Aircraft flight lines for the four flights of the ROWS instrument during the St. Valentine's Day wind/wave event showing also the SWADE data buoy locations and the current fields from the U.S. Navy's Operational Gulf Stream Forecasting System (NOGUSFS) for the dates indicated. The "S" file identifications are for the radar wave spectrum observations and the "A"



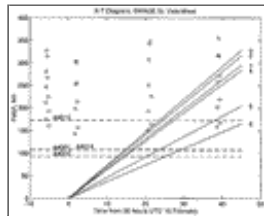
[Click on thumbnail for full-sized image.](#)

Fig. 1. (*Continued*) file identifications are for the ROWS altimeter mode observations of wind speed. Note that the current fields in the central portions of the maps are displaced slightly to the south relative to their actual positions because a different map projection was used for the current fields.



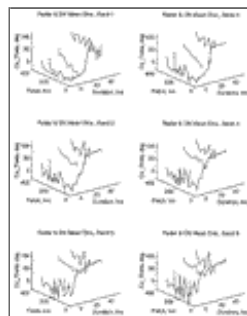
[Click on thumbnail for full-sized image.](#)

Fig. 2. Neutral equivalent 10-m wind speeds and wind directions for five SWADE data buoys with time periods of the radar flights indicated by vertical dashed lines. The curves in both panels that show a discontinuity around day number 14.75 are for buoy number 44015 (Discus-E).



[Click on thumbnail for full-sized image.](#)

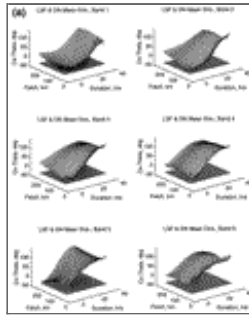
Fig. 3. Locations of radar (circles) and buoy (dashed lines) data points in fetch (x) and duration (t) coordinates. Wave data from the directional wave buoys 44001 (Discus-N) and 44023 (Discus-C) only are used in the present study. The six lines emanating from $(x, t) = (0, 0)$ are characteristics of mean direction propagation for the six analysis frequency bands based on a mean advection velocity $\langle V_{\theta} \cos \theta \rangle$ from the radar data for 15 February. The band center frequencies are given in [Table 1](#).



[Click on thumbnail for full-sized image.](#)

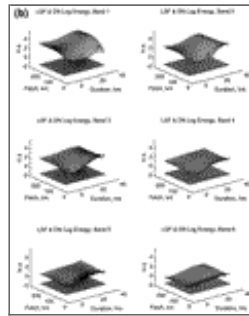
Fig. 4. Radar and Discus-N raw mean direction data for the six analysis frequency bands indicated. The buoy data are the traces at approximately 100-km fetch, and the radar data traces for the four aircraft flights run orthogonal to this trace. The data

are plotted in terms of the complement “co-theta” of the mean direction θ relative to the x axis, which is normal to the coastline. Co-theta = 0 is thus directed northward, parallel to the coastline.



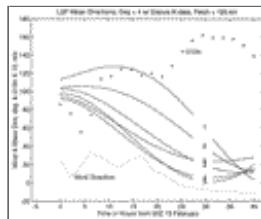
Click on thumbnail for full-sized image.

Fig. 5. Least squares fitted mean direction (a) and log energy (b) surfaces for combined radar and Discus-N data for the six frequency bands indicated with the Discus-N raw data trace shown for comparison. The degree of the fit polynomial is four.



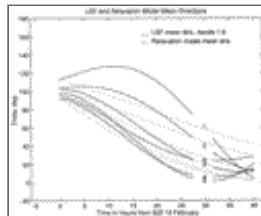
Click on thumbnail for full-sized image.

Fig. 5. (Continued)



Click on thumbnail for full-sized image.

Fig. 6. Smoothed temporal responses from a constant fetch cut through the least squares fit surfaces of mean direction in Fig. 5a. The analysis fetch is 195 km. The wind speed and direction data are from the five-buoy vector average. The numbers on the curves are the frequency band numbers.



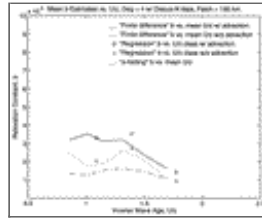
Click on thumbnail for full-sized image.

Fig. 7. Relaxation model solution (8) for the mean wave direction in the case of a step function wind shift compared to the smoothed temporal response curves shown in Fig. 6.



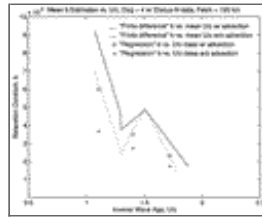
[Click on thumbnail for full-sized image.](#)

Fig. 8. Differential estimates of the directional relaxation parameter b_t vs time in the event relative to 0000 UTC 15 February. (a) Case A2: Fourth-degree polynomial fit with Discus-N data and 5-buoy average winds for a fetch of 195 km with no constraints applied. (b) Case B2: Same as case A2 but subject to the constraints B1–B3.



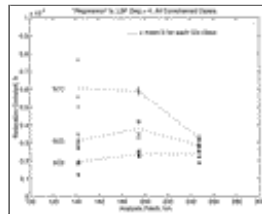
[Click on thumbnail for full-sized image.](#)

Fig. 9. Comparison of finite difference, regression, and e -folding estimates of the relaxation parameter for the unconstrained data case A2, with and without advection correction.



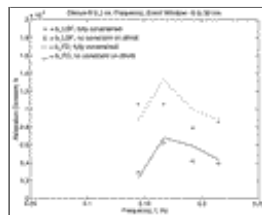
[Click on thumbnail for full-sized image.](#)

Fig. 10. Finite difference and regression estimates for the constrained data case B2, with and without advection correction.



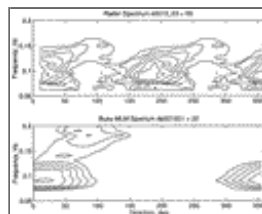
[Click on thumbnail for full-sized image.](#)

Fig. 11. Summary of individual case results B1–B12 for constrained regression estimates of the relaxation parameter b_{LSF} with advection correction for the three inverse wave age (U/c) classes plotted against the analysis fetch.



[Click on thumbnail for full-sized image.](#)

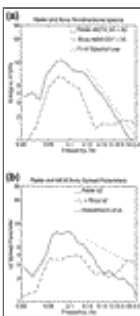
Fig. 12. Comparison of relaxation parameter estimates b_t from the buoy data alone with and without the positivity requirement $b \geq 0$ being in effect.



[Click on thumbnail for full-sized image.](#)

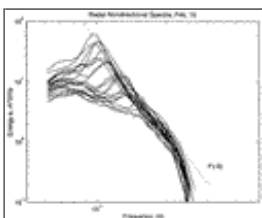
Fig. A1. Comparison of radar (upper panel) and Discus-E (lower panel) directional spectra for 15 February (midevent) for

comparable fetch. The radar spectrum is the average of files S03 and S09 north and south of Discus-E; the buoy spectrum is the average of 2100 and 2200 UTC observations. The contour levels are in steps of 1.5 dB.



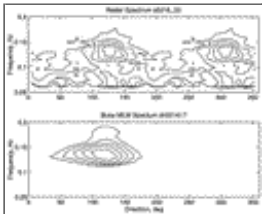
[Click on thumbnail for full-sized image.](#)

Fig. A2. Nondirectional energy spectra (a) and spread parameters (b) corresponding to the directional spectra of [Fig. A1](#). Solid line is radar data and dashed line is Discus-E data. The dotted line in the upper panel is the f^{-4} power law given by [Eq. \(A1\)](#) with a buoy-observed neutral wind speed of 11.8 m s^{-1} . The buoy spread parameter is derived from the buoy MLM distribution; the dotted curve is the [Hasselmann et al. \(1980\)](#) spreading law (see §C).



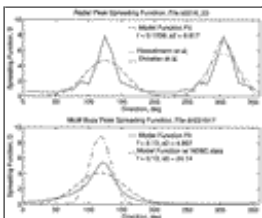
[Click on thumbnail for full-sized image.](#)

Fig. B1. All radar-inferred nondirectional energy spectra $\mathcal{E}(f)$ for 16 February (22 fetch-limited spectra). Noise background subtraction is modified Rayleigh noise. The dotted curve is the f^{-5} law for the envelope with the Phillips constant $\beta = 8.1 \times 10^{-3}$.



[Click on thumbnail for full-sized image.](#)

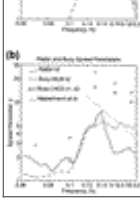
Fig. B2. Comparison of approximately collocated radar (upper panel) and Discus-N (lower panel) directional spectra for February 16 (end event). Contouring is in 3-dB decrements from the respective peaks.



[Click on thumbnail for full-sized image.](#)

Fig. B3. Comparison of radar (upper panel) and buoy (lower panel) directional distributions (times π and 2π , respectively) for peak frequencies of the directional spectra of [Fig. B2](#). Solid curves are the observed distributions. In the buoy case, the “observed” distribution is according to the maximum likelihood method of distribution estimation. The dashed curves are the cosine-power model functions [\[Eq. \(C1\)\]](#) respectively derived from the second harmonics of the two observed distributions. The dash-dot curve for the buoy plot is the cosine power model function corresponding to the NDBC second harmonic data ($s_2 = 24.1$). In the right half-space of the radar plot the model distributions of [Hasselmann et al. \(1980\)](#) and [Donelan et al. \(1985\)](#) are plotted [\[Eqs. \(C2\) and \(C3\)\]](#).





Click on thumbnail for full-sized image.

Fig. B4. Comparison of radar and buoy nondirectional spectra \mathcal{E} (a) and directional spread parameters s (b) for the example directional spectra of Fig. B2. Solid curves are radar data and dashed curves are buoy data. In (b) the dashed curve is s_2 from the buoy MLM distribution; the circles and crosses are, respectively, s_1 and s_2 derived from NDBC harmonic coefficient data.

The dotted curve in (a) is the f^{-4} law for the rear face region, Eq. (A1), with a buoy observed neutral wind speed of 14.8 m s^{-1} ; in (b) the dotted curve is the Hasselmann s_1 spreading law, Eq. (C2).

Corresponding author address: Dr. Robert E. Jensen, U.S. Army Corps of Engineers, Engineer Research and Development Center, 3909 Halls Ferry Road, Vicksburg, MS 39180-6199.

E-mail: jensen@madmax.wes.army.mil

top ▲



© 2008 American Meteorological Society [Privacy Policy and Disclaimer](#)
 Headquarters: 45 Beacon Street Boston, MA 02108-3693
 DC Office: 1120 G Street, NW, Suite 800 Washington DC, 20005-3826
amsinfo@ametsoc.org Phone: 617-227-2425 Fax: 617-742-8718
[Allen Press, Inc.](#) assists in the online publication of AMS journals.